The Role of the Human Brain Neuron-Glia-Synaptic Composition in Forming Resting State Functional Connectivity Networks

Sayan Kahali[a], Marcus E. Raichle[a,b] and Dmitriy A. Yablonskiy[a*]
[a]Department of Radiology, Washington University School of Medicine, St. Louis, MO 63110, USA
[b]Department of Neurology, Washington University School of Medicine, St. Louis, MO 63110, USA

*Corresponding author:
Dmitriy A. Yablonskiy, PhD
Mallinckrodt Institute of Radiology, Washington University, 4525 Scott Ave. Room 3216
St. Louis MO, 63110
Email: yablonskiyd@wustl.edu
https: BMRL-DmitriyYablonskiy
Tel.: +1(314)362-1815; Fax: +1(314)362-0526

Key words: functional connectivity, hierarchy of functional networks, brain cellular circuits, quantitative Gradient Recalled Echo MRI, neurons, glia cells, synapses

ABSTRACT

While significant progress has been achieved in studying resting state functional networks in a healthy human brain and in a wide range of clinical conditions, many questions related to their relationship to the brain's cellular constituents remain open. In this paper we use quantitative Gradient Recalled Echo (qGRE) MRI for in vivo quantitative mapping of human brain cellular composition, and BOLD (blood oxygen level dependent) MRI resting state data from the Human Connectome Project to explore how the brain cellular constituents relate to resting state functional networks. Our results show that the BOLD-signal-defined synchrony of connections between cellular circuits in network-defined individual functional units is mainly associated with the regional neuronal density, while the strength of the functional connectivity between functional units is influenced not only by the neuronal but also glia and synaptic components of brain tissue cellular constituents. Data show that these cellular-functional relationships are most evident in the infra-slow frequency range (0.01–0.16 Hz) of brain activity, which is known to be linked with fluctuations of the BOLD signal. These mechanisms lead to a rather broad distribution of resting state functional network properties. We found that visual networks with the highest neuronal density (but lowest density of glial cells and synapses) exhibit the strongest coherence of BOLD signal in individual functional units, as well as the strongest intra-network connectivity. The Default Mode Network (DMN) is positioned near the opposite part of the spectrum with relatively low coherence of the BOLD signal but a remarkably balanced cellular content enabling DMN prominent role in the overall organization of the brain and the hierarchy of functional networks in health and disease.

INTRODUCTION

Resting state functional brain connectivity has become an established area of research in the arena of cognitive neuroscience and its related applications. Functional connectivity refers to the statistical correlation between temporally coherent low-frequency spontaneous fluctuations of the resting state functional MRI (rs-fMRI) signal in different brain regions (1) and provides insights into large-scale brain circuit organization (2,3). The rs-fMRI signal is–acquired with MRI sequences sensitive to the Blood Oxygen Level Dependent (BOLD) effect (4) and identifies consistent resting-state networks (5-7) that play important roles in normal brain function and various neurological conditions such as: normal aging (8) and Alzheimer's disease (9).

An important question in understanding the physiological basis of resting state functional connectivity is its relationship to brain structural connectivity. In the human brain this issue is usually addressed by studying trajectories of brain white matter (WM) tracts with Diffusion Tensor Imaging (DTI) tractography (10-13). However, the direct structural connectivity through WM is not the sole mechanism underlying functional connectivity (14) (15).

While DTI is sensitive to structural connections governed by WM tracts, it does not usually have enough sensitivity to resolve existing neuronal connections through the brain cortical regions, which are characterized by a complex network of interconnected and intersected neuronal processes (axons and dendrites). It is also understood that functional connectivity of the brain is not uniquely dependent on the neurons, it also relies on glial cells which significantly influence structural and functional connectivity (16), providing metabolic and regulatory support for neurons (17,18) (19). Astrocytes are responsible for increasing the amount of mature and functional synapses (17,18). Moreover, neuron-glia cross-talk leads to synaptic formation and remodeling (20). It has also been observed that neurons generate weak synapses in the absence of glia (17,21). Hence, incorporating information on cellular composition into brain structural connectivity can provide crucial information for our understanding of brain functional connectivity network formation and functioning.

In this paper, to identify brain cellular structure we use data obtained by means of quantitative Gradient Recalled Echo (qGRE) MRI technique (22). The qGRE method is based on the gradient recalled echo MRI with multiple gradient echoes and data analysis allowing separation of tissue cellular specific (R2t*) GRE signal relaxation from relaxation caused by the *baseline* BOLD (blood oxygen level dependent) mechanism (4,23) and adverse effects of magnetic field inhomogeneities (24) corrected using a VSF (voxel spread function) method (25). We also use a quantitative relationships established in Wen et al. (26) between brain cellular composition and the R2t* metric of the qGRE MRI signal. Based on the analysis of the genetic information from the Allen Human Brain Atlas, Wen et al. (26) identified several networks of gene expression profiles coherently expressed across brain anatomical structures and established their association with the R2t* metric of the qGRE signal in these structures. Data showed the strongest association between R2t* and genes that are associated with ion channels primarily distributed along neuronal processes, including axons (myelinated and not myelinated) and dendrites which typically occupy over 85% of the space comprised by neurons. Noting these findings, it was demonstrated (26) that the in vivo R2t* measurement largely reflects a transcriptional correlate for major parts of the neuronal cell bodies and processes, thus representing the neuronal contribution to brain tissue cellular composition. Moreover, a quantitative relationship between the R2t* metric of the qGRE signal in a healthy human

brain cortical Grey Matter (GM) and a neuronal density index Y_{neuron} that serves as a proxy for the brain tissue neuronal density was established in (26):

$$R2t^{*} = 5.8 + 20.4 \cdot Y_{neuron} \quad [1]$$

where R2t* is measured in sec^{-1} and the neuronal density index Y_{neuron} is a dimensionless parameter ($0 < Y_{neuron} < 1$) proportional to the tissue neuronal density. This relationship is illustrated in Appendix Figure A1. Further analysis (26) also established relationships in healthy human brain cortical GM between Y_{neuron} and indices characterizing densities of glia cells (Y_{glia}) and synapses ($Y_{synapse}$):

$$Y_{glia} / Y_{neuron} = 0.38 \cdot Y_{neuron}^{-1.38}; \quad Y_{synapse} / Y_{neuron} = 0.34 \cdot Y_{neuron}^{-1.51} \quad [2]$$

thus, corroborating previous histology-based reports (27,28) that healthy human brain regions with higher neuronal density have relatively low densities of glia cells and synapses. Herein we combine qGRE-derived brain cellular information with resting state BOLD data from the Human Connectome Project (HCP) to establish a quantitative relationship between resting state functional connectivity and human brain cortical cellular composition. We show that while the synchrony of the brain cellular circuits in network-defined functional units is mainly associated with the regional neuronal density, the strength of the inter-unit within-network functional connectivity has significant association not only with units' neuronal content but also with their glia and synaptic constituents. These cellular-functional associations are most prominent in the infra-slow frequency range (0.01 – 0.16 Hz) of brain activity as determined by the BOLD signal.

METHODS

The functional connectivity data were obtained from the HCP1200 dataset (February, 2017 release). The qGRE data were obtained from 16 healthy control participants, with local IRB approval from Washington University in Saint Louis. Written informed consent was obtained from all participants.

Resting State Functional Connectivity Data

The HCP1200 dataset was recorded on young adults aged between 22-35 (5). In this study, we used 183 subjects (about 20% of total available) that had 4, 15-minute RS-fMRI scans. The fMRI scans were preprocessed using HCP structural (PreFreeSurfer, FreeSurfer, and PostFreeSurfer) and functional (fMRIVolume and fMRISurface) pipelines. The ICA+FIX pipeline was applied to refine the rs-fMRI data to regress out the spatially specific temporal artefacts, i.e., scanner artefacts, subject movement, breathing and cardiac pulsation. The fMRI data were then summarized in 91,282 grayordinates which are cortical grey matter surface vertices and subcortical grey matter voxels(29). The data in each grayordinate obtained from 4 scans of each subject (1200 timepoints ×4 runs) were concatenated after performing de-meaning and variance normalization. The concatenated time series data for each subject were grouped into 300 parcels (i.e., functional units) using Schaefer's et al. (30) local-global parcellation of the cortical grey matter identified by employing the gradient-weighted Markov Random Field (gwMRF) model which fuses local gradient and global similarity approaches. Signals from these time-series data for all vertices in each parcel were averaged together and each parcel for further analysis was represented by a single signal (1200 timepoints ×4 runs). The parcellated time-series data for each of 183 subjects were concatenated together for time domain network analysis (1200 timepoints ×4 runs × 183 subjects).

To represent the resting state functional *BOLD signal from each individual functional unit* (*designated below as Region Of Interest, i.e. ROI*) we calculated the Standard Deviation (STD_i) of the average signals combined from individual vertices in each functional unit *i* (*i* =1, 2, …, 300). Due to normalization, the *STD* of each signal from the vertices is equal to one, such that the STD_i of the combined signal represents *the coherence* of the individual signals in the ROI (*STD* = 1 if signals from vertices are coherent, and *STD* = 0 in there is no correlation between them). Then we represent the BOLD signal coherence for each network as a mean value of STD_i of all ROI_i belonging to a given network:

$$BOLD\ Signal\ Coherence_n = mean\left\langle STD_i \right\rangle; n = 1,2,...,17 \quad [3]$$

The resting state functional Connectivity Strength ($CS_{i,j}$) between two ROIs (*i* and *j*) is calculated as a Pearson Correlation Coefficient between two time series data from ROI_i and ROI_j, each having 1200 timepoints × 4 runs x 183 subjects.

To characterize the intra-network connectivity, we introduce the *intra-Network Connectivity Strength* NCS_n by calculated weighted average $CS_{i,j}$ between all ROIs belonging to a given network:

$$NCS_n = mean\left\langle CS_{i,j} \right\rangle_{i \neq j}; n = 1,2,...,17 \quad [4]$$

Since ROIs contain different number of vertices, all ROIs in this calculation are weighted by the number of corresponding vertices.

The frequency content of rs-fMRI signal was analyzed by converting the time-series data to frequency domain by performing a Fourier transformation on time-series data from each ROI independently, for each session per subject. The Fourier transformed data were then averaged across all sessions and all subjects, before separation into preselected frequency bins of 0.014 Hz and 0.0047 Hz. Each bin was then converted back to the time domain using inverse Fourier transform.

Quantitative Gradient Recalled Echo (qGRE) MRI Data Analysis

To identify brain cellular structure we used data obtained by means of quantitative Gradient Recalled Echo (qGRE) MRI technique (22). The qGRE method is based on the gradient recalled echo MRI with multiple gradient echoes and data analysis allowing separation of tissue cellular specific (R2t*) GRE signal relaxation, from relaxation caused by the baseline Blood Oxygen Level Dependent (BOLD) mechanism and adverse effects of magnetic field inhomogeneities (24). We used MRI data obtained from 16 healthy volunteers aged between 23-35 from a previously published study (31). These volunteers were not a part of the HCP sample, but their age range was selected to match HCP resting state functional MRI data. In Zhao et al., (31) MRI image data were obtained using a 3T Trio MRI scanner (Siemens, Erlangen, Germany) using a 32-channel phased-array RF head coil. Data acquisition was done by means of 3D Gradient Recalled Echo (GRE) MRI sequence with 10 gradient echoes, followed by a navigator for correcting physiological fluctuations (32). The sequence parameters were flip angle (FA) = 30°, repetition time (TR) = 50 ms, first echo time (TE_1) = 4 ms, echo spacing ΔTE = 4 ms, voxel size of 1 × 1 × 2 mm^3 and acquisition time of 11 minutes. Field inhomogeneity effects were corrected using a Voxel Spread Function (VSF) method (33).

Data analysis was performed with a stand-alone computer with in-house developed programs written in MatLab (MathWorks Inc., Natick, MA, USA). After phase correction, k-space data from each radio

frequency (RF) channel were converted to the spatial domain, and the 3D spatial Hanning filter was applied to reduce Gibbs ringing artifacts and signal noise. To achieve optimal model parameter estimations, the multi-channel data (ch = 1, 2, …, M) were combined according to the following algorithm allowing the most accurate model parameters evaluation (34,35):

$$S_n\left(TE\right)=\sum_{ch=1}^{M}\lambda_{ch}\cdot\overline{S}_n^{ch}\left(TE_1\right)\cdot S_n^{ch}\left(TE\right),\quad \lambda_{ch}=\frac{1}{M\cdot\varepsilon_{ch}^2}\sum_{ch'=1}^{M}\varepsilon_{ch'}^2 \qquad [5]$$

Where $\overline{S}$ denotes the complex conjugate of S; index n represents the voxel position in space; λ_{ch} are weighting factors, and ε_{ch} are noise amplitudes (r.m.s.).

A theoretical model of BOLD (blood oxygen level dependent) contrast (23) was used to differentiate the contribution of tissue-cellular-specific relaxation (R2t*) and BOLD contributions to the total R2* relaxation:

$$S(TE_n)=A_0\cdot\exp\left[-R2t^*\cdot TE_n-\zeta\cdot f_s(\delta\omega\cdot TE_n)-i\cdot\varphi-i\cdot 2\pi\cdot\Delta f\cdot TE_n\right]\cdot F(TE_n) \qquad [6]$$

where A_0 is the signal amplitude; $\delta\omega$ is the characteristic frequency determined by the susceptibility difference between deoxygenated blood and surrounding tissue; ζ is the volume fraction of deoxygenated blood; nonlinear function $f_s\left(\delta\omega\cdot TE\right)$ accounts for the BOLD effect (23); φ and Δf are phase and frequency shifts (dependent on tissue structure and also macroscopic magnetic field created mostly by tissue/air interfaces), and the function $F(TE_n)$ describes the effect of macroscopic magnetic field inhomogeneities (36). Herein, $F(TE_n)$ was calculated by a voxel spread function (VSF) method (25) and we used a mathematical expression for the function f_s in terms of a generalized hypergeometric function (37) ${}_1F_2$:

$$f_s(\delta\omega\cdot TE)={}_1F_2\left(\left[-\frac{1}{2}\right];\left[\frac{3}{4},\frac{5}{4}\right];-\frac{9}{16}(\delta\omega\cdot TE)^2\right)-1 \qquad [7]$$

Structural Connectivity Analysis Based on qGRE-Defined Brain Cellular Structure

For our analysis, the R2t*-based calculated cellular indices (Y_{neuron}, Y_{glia} and $Y_{synapse}$), Eqs. [1] and [2], were projected on the cortical surface through the surface-based registration using the grayordinates. The grayordinates were combined to 300 parcels based on the Schaefer's et al. parcellation (30).

To establish a contribution of the cellular composition of two connected ROIs (*i* and *j*) to their $CS_{i,j}$, we consider six *structural connectivity* matrices accounted for six types of connections (neuron-neuron, glia-glia, synapse-synapse, neuron-glia, neuron-synapse, and glia-synapse) defined on 300 ROIs:

$$\begin{aligned}&\hat{Y}_{neuron-neuron}=\left\langle Y_{neuron}^i\times Y_{neuron}^j\right\rangle;\quad \hat{Y}_{glia-glia}=\left\langle Y_{glia}^i\times Y_{glia}^j\right\rangle;\quad \hat{Y}_{synapse-synapse}=\left\langle Y_{synapse}^i\times Y_{synapse}^j\right\rangle;\\&\hat{Y}_{neuron-glia}=\left\langle Y_{neuron}^i\times Y_{glia}^j+Y_{glia}^i\times Y_{neuron}^j\right\rangle;\hat{Y}_{neuron-synapse}=\left\langle Y_{neuron}^i\times Y_{synapse}^j+Y_{synapse}^i\times Y_{neuron}^j\right\rangle;\\&\hat{Y}_{glia-synapse}=\left\langle Y_{glia}^i\times Y_{synapse}^j+Y_{synapse}^i\times Y_{glia}^j\right\rangle\end{aligned} \qquad [8]$$

For each network we also introduce *internal (intra-network) structural connectivity strength* for six types of connections:

$$Y^n_{neuron-neuron};\quad Y^n_{glia-glia};\quad Y^n_{synapse-synapse};\qquad Y^n_{neuron-glia};\quad Y^n_{neuron-synapse};\quad Y^n_{glia-synapse};\ n=1,2,...,17 \quad [9]$$

where each Y^n is calculated as a *weighted average* $Y_{i,j}$ ($i \neq j$) in Eq. [8] across all connections in the n-th network. All ROIs in these calculations are weighted by their number of voxels.

Analysis based on T1w/T2w approach

To further understand the role that different parts of the neuron play in formation of brain functional connectivity, we can compare our R2t*-based results with a ratio of T1-weighted (T1w) to T2-weighted (T2w) images as a proxy related to cortical tissue myelin content proposed by Glasser and Van Essen (38). While this proxy does not represent a quantitative measure of myelin content, for example as discussed in (39), it was successfully used for mapping cytoarchitecture of human cortical areas (40). By using T1w and T2w data from the same HCP subjects that are used in this paper for rs-fMRI analysis, we have calculated a Myelin Index ($Y^n_{myelin}; n=1,2,...,17$, as a ratio of T1w to T2w images) for all ROIs in Yeo's networks. Similar to Eq. [9], we have also introduced corresponding connectivity indices characterizing each network: $Y^n_{myelin-myelin}; n=1,2,...,17$.

RESULTS

The Strength of Resting State Functional Networks is Significantly Associated with the Neuron-Neuron, Neuron-Glia and Neuron-Synaptic Structural Circuits in the Human Brain Cortex

In this paper we provide data analysis based on a structure of 300 gwMRF ROIs combined in 17 resting-state networks developed by Yeo et al (7,30). These networks are presented in Figure 1. We have selected a gwMRF brain parcellation scheme (30) because it exhibits an improved functional connectivity homogeneity compared with other parcellations (40-43) and provides a sufficient number of parcels to delineate brain cortical anatomical structures as discussed by Van Essen et al. (44).

Using qGRE data we have analyzed the contribution of magnetic field inhomogeneities in signal formation of all 17 networks and found that the two limbic networks are affected the most. In fact, the signals from the networks Limbic A and Limbic B had more than 88% and 80% of voxels significantly affected by the background magnetic field inhomogeneities, respectively, while all other networks had on average only 9% of "bad" voxels (see Appendix Figure A2 for details). Consequently, we omitted limbic networks from further consideration.

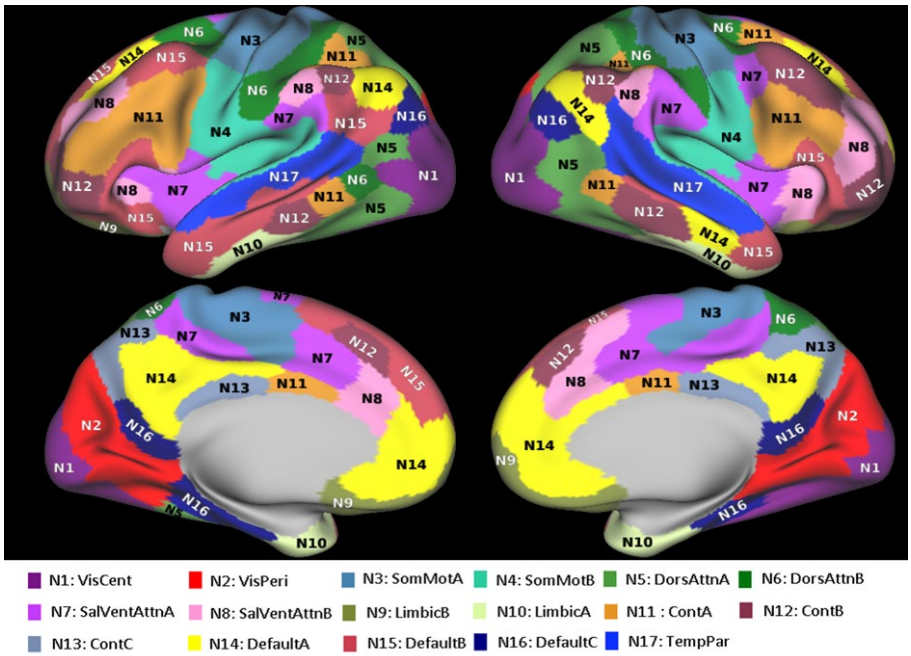

Figure 1. Network parcellation of Yeo's 17-networks. The 17-networks include the following regions: N1: VisCent - Visual A (22 ROIs), N2: VisPeri - Visual B (18 ROIs), N3: SomMotA - Somatomotor A (30 ROIs), N4: SomMotB - Somatomotor B (21 ROIs), N5: DorsAttnA - Dorsal Attention A (16 ROIs), N6: DorsAttnB - Dorsal Attention B (16 ROIs), N7: SalVentAttnA - Salience/Ventral Attention A (25 ROIs), N8: SalVentAttnB - Salience/ Ventral Attention B (14 ROIs), N9: LimbicB - Limbic B (9 ROIs), N10: LimbicA - Limbic A (11 ROIs), N11: ContA - Control A (22 ROIs), N12: ContB - Control B (18 ROIs), N13: ContC - Control C (8 ROIs), N14: DefaultA - Default A (23 ROIs), N15: DefaultB - Default B (25 ROIs), N16: DefaultC - Default C (10 ROIs), N17: TempPar - Temporal Parietal (12 ROIs). Further details on networks' structure can be found in (7,30).

The theoretical approach described in the Methods section allows – based on Eqs. [1] and [2] – the calculation of neuronal, synaptic, and glia cells indices (qGRE proxy parameters proportional to the neuronal, synaptic, and glia cells densities) for each network. The R2t* maps were obtained from 16 healthy volunteers aged 23 to 35 as described in the Methods section, projected on 300 selected ROIs and averaged together. **Table A** in the Appendix shows variation of R2t* measurements across the subjects. Images representing neuronal, glia and synaptic density indices are presented in **Figure 2**.

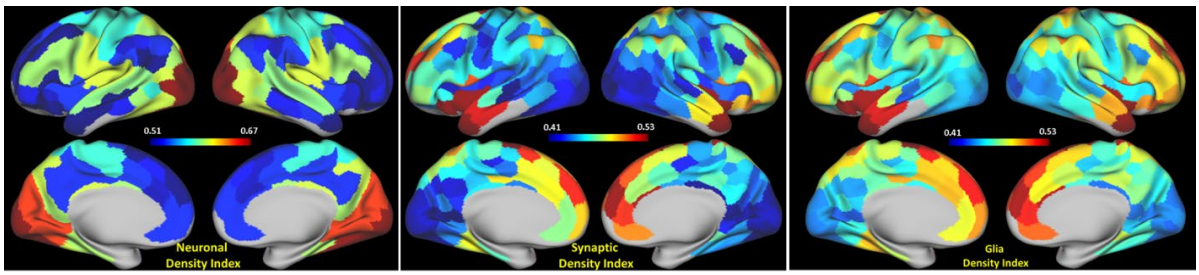

Figure 2. Surface maps of neuronal, glia and synaptic density indices (qGRE proxy for the neuronal, synaptic and glia cells densities) for 15 networks. Data representing the results in this figure are shown in the Appendix **Table A**.

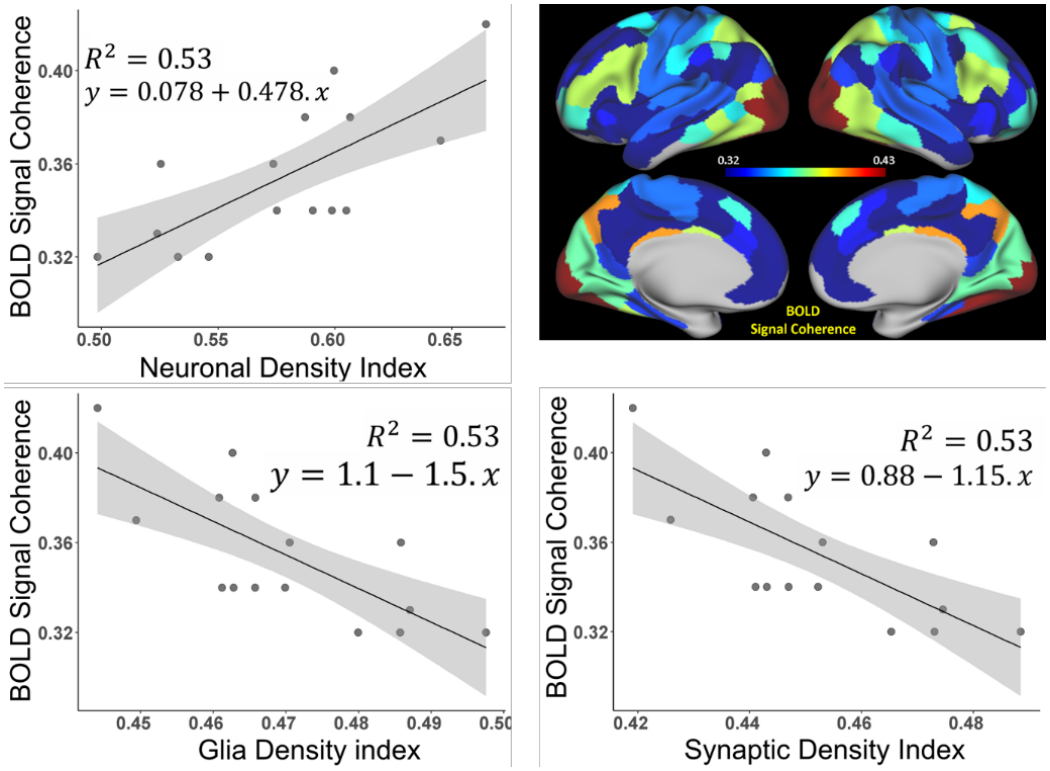

Figure 3. Association between BOLD signal coherence in 15 networks and neural, glia, and synaptic density indices in these networks (limbic networks are omitted). Neuronal (Y_{neuron}), glia (Y_{glia}), and synaptic ($Y_{synapse}$) density indices were calculated from R2t* values using Eqs.[1] and [2] and then averaged for each network. Shaded areas – 95% confidence intervals. The R^2 values for all three correlations are practically identical because of previously established correlated spatial distribution of neurons, glia, and synapses in the healthy human cortex (27,28) which is reflected by the relationship between glia (Y_{glia}) and synaptic ($Y_{synapse}$) indices to the neuronal index (Y_{neuron}) by means of Eq. [2].

Plots in **Figure 3** represent correlation between BOLD signal coherence in 15 networks and neural, glia, and synaptic density indices in these networks. Data show strong positive association with mean neuronal density index and negative association with glia and synaptic density indices. *This means that neurons, not glia cells and synapses, are mostly responsible for the coherence of the BOLD signal.* The strong negative association of BOLD signal coherence with glia and synaptic density indices is due to the fact that the densities of glial cells and synapses are negatively associated with neuronal density in the corresponding regions as presented in Eq. [2].

Even though the strength of the BOLD signal coherence in functional networks is mostly associated with the networks' neuronal content (**Figure 3**), the functional connectivity of the brain is not solely dependent on the neurons, it also includes glial cells (Astrocyte, Microglia, Oligodendrocytes) which significantly influence structural and functional connectivity governed by neurons (16). Obviously, the factors defining the strength of functional connectivity between two ROIs are the actual neuronal pathways connecting these ROIs and the cellular composition of these ROIs. Herein we focus on the latter – the ROIs' cellular composition.

Data in **Figure 4** show correlations between the *intra-Network Connectivity Strength, NCS_n,* Eqs. [8] and [9] and the structural connectivity strength Y^n of these networks for six types of cellular connections (neuron-neuron, glia-glia, synapse-synapse, neuron-glia, neuron-synapse, and glia-synapse). Data illustrates that the neuron-neuron ($\boldsymbol{Y}_{neuron\text{-}neuron}$), neuron-glia ($\boldsymbol{Y}_{neuron\text{-}glia}$) and neuron-synapse ($\boldsymbol{Y}_{neuron\text{-}synapse}$) connections show strong positive correlations suggesting these connections as dominant features contributing to the inter-ROIs resting state functional connectivity.

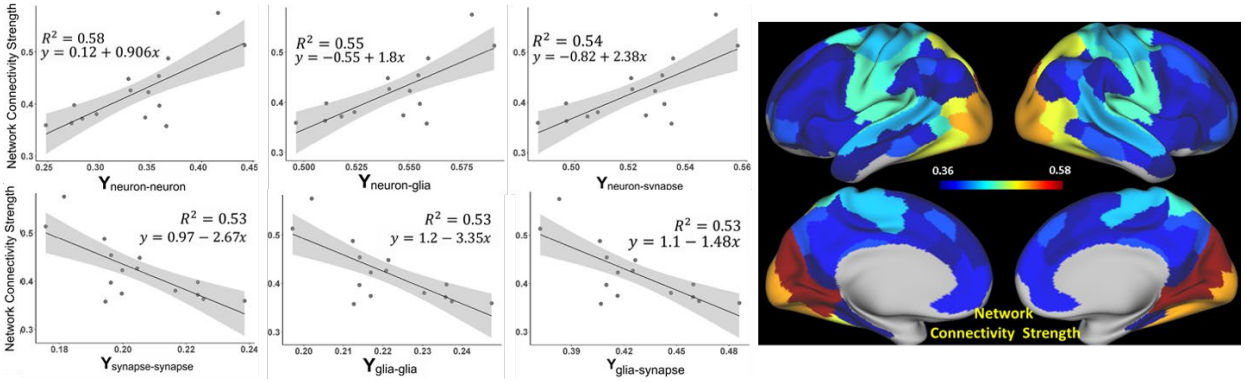

Figure 4. Association between Network Connectivity Strength (NCS) and structural connectivity between neurons, synapses, and glia cells. Plots show correlations between resting state network connectivity strength NCS_n and structural connectivity strength Y^n (index ^{n} is omitted in the figure) of these networks for six types of cellular connections (neuron-neuron, glia-glia, synapse-synapse, neuron-glia, neuron-synapse, and glia-synapse) for 15-networks. Shaded areas – 95% confidence intervals. Images represent surface maps of NCS for 15 networks.

While data in **Figure 3** and **Figure 4** show network-wide associations between the BOLD signal coherence vs. neural density index and network connectivity strength vs. structural connectivity between cells, respectively , **Figure A3** in the Appendix shows similar associations based on 280 individual ROIs (limbic-network-associated ROIs were excluded), which are highly significant (p= E-11 and E-98 correspondingly).

We have also tested for the randomness of our correlation result in **Figure 3** (BOLD signal coherence vs. Neuronal Density Index) and **Figure 4** (Functional Connectivity (FC) vs. structural connectivity between neurons) by means of permutation test (randomization test). The permutation test for BOLD signal coherence vs. Neuronal Density Index was done by randomly permuting BOLD signal coherence 10000 times and calculating correlation with Neuronal Density Index for each permutation. The curve in **Figure A4 (b)** in the Appendix illustrates the distribution of obtained *r*-values validating a significant difference with p-value < 0.000001). Similarly, the functional connectivity strengths between 280 ROIs (excluding Limbic networks) were randomly permuted 20000 times and correlated with the structural connectivity between neurons for each permutation. The curve in the **Figure A4 (a)** in the Appendix shows the distribution of obtained *r*-values, thus validating a significant difference (p-value < 0.000001).

To demonstrate statistical sufficiency of our sample size (N=183) we ran analyses similar to those presented in **Figure 3** and **Figure 4**, using a smaller sample size (N = 100). Results presented in Appendix **Figure A5** show practically the same correlations, with only slightly smaller R^2 values.

Data in Figure **5** show associations between cortical tissue Myelin Index calculated based on the ratio of T1w/T2w images and qGRE-based calculated Neuronal Density Index (**Figure 5a**), BOLD signal Coherence (**Figure 5b**), and Network Connectivity Strength (**Figure 5c**).

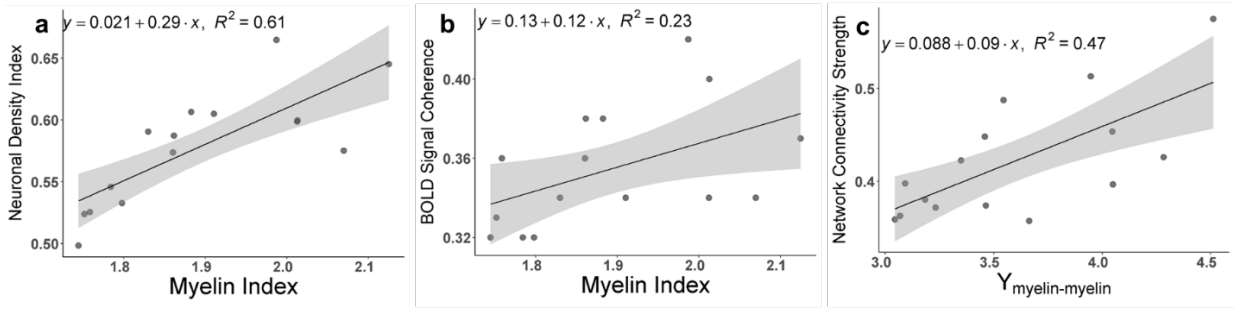

Figure 5. Association between qGRE and T1w/T2w –results based on 15 networks. **(a)** Correlation between Neuronal Density Index and Myelin Index. Points represent average values for individual networks. Shaded areas – 95% confidence intervals. Myelin Index was calculated based on T1w/T2w images. **(b)** Correlations between the strength of the BOLD signal coherence and average Myelin Index in the networks. **(c)** Correlation between resting state intra-network connectivity strength, NCS and structural connectivity strength calculated based on the myelin indexes in the connected ROIs (similar to that described by Eqs. [4], [8]).

Brain cortical cellular composition shows the strongest association with the resting state BOLD signal coherence and network connectivity in the infra-slow frequency range of neuronal activity

Data in **Figure 3** show that the BOLD signal coherence varies significantly among networks and strongly correlates with the networks' neuronal density. Similar behavior is seen for network connectivity strength which also depends on the brain cellular composition, though in a different manner; the intra-network connectivity strength shows the strongest correlation with intra-network neuron-neuron, neuron-synaptic, and neuron-glia connections between network's ROIs. These results were obtained by analyzing the time courses of rs-fMRI signal without accounting for frequency content of this signal. At the same time, only the infra-slow (below 0.1 Hz) frequency fluctuations of the resting state BOLD signal are usually considered as a signature of the neuronal activity (3,45-49). To investigate the detailed relationship between cellular composition and frequency components of the resting state BOLD signal, we converted the time series data into 50 consecutive frequency bands covering frequency domain 0.01-0.60 Hz (see methods section) and analyzed different frequency components independently. The results for 15 networks are presented in **Figure 6**. **Figure 6a** shows the BOLD signal coherence (mean standard deviation of the rs-fMRI signal) in each network as a function of the rs-fMRI signal frequency. We found that while different networks exhibit different signal strength coherence, the general trend is quite similar – the strongest coherence of BOLD signal fluctuations is present in the frequencies below 0.16 Hz, with the peak between 0.01-0.03 Hz. The NCS calculated in terms of the mean intra-network correlation coefficient for each of the 15 networks as a function of rs-fMRI signal frequency content is seen in **Figure 6b,** which also displays increased connectivity strengths in a similar frequency range below 0.16 Hz, with the peak between 0.01-0.03 Hz**. Figure 6c** shows correlation between BOLD signal coherence in 15

networks and the tissue neuronal content of these networks (as in **Figure 3**) as a function of the rs-fMRI signal frequency. Interestingly, the strongest correlation exists not only in the frequency range where the BOLD signal coherence and NCS are the strongest, but in a rather broad infra-slow frequency range between 0.01 – 0.16 Hz.

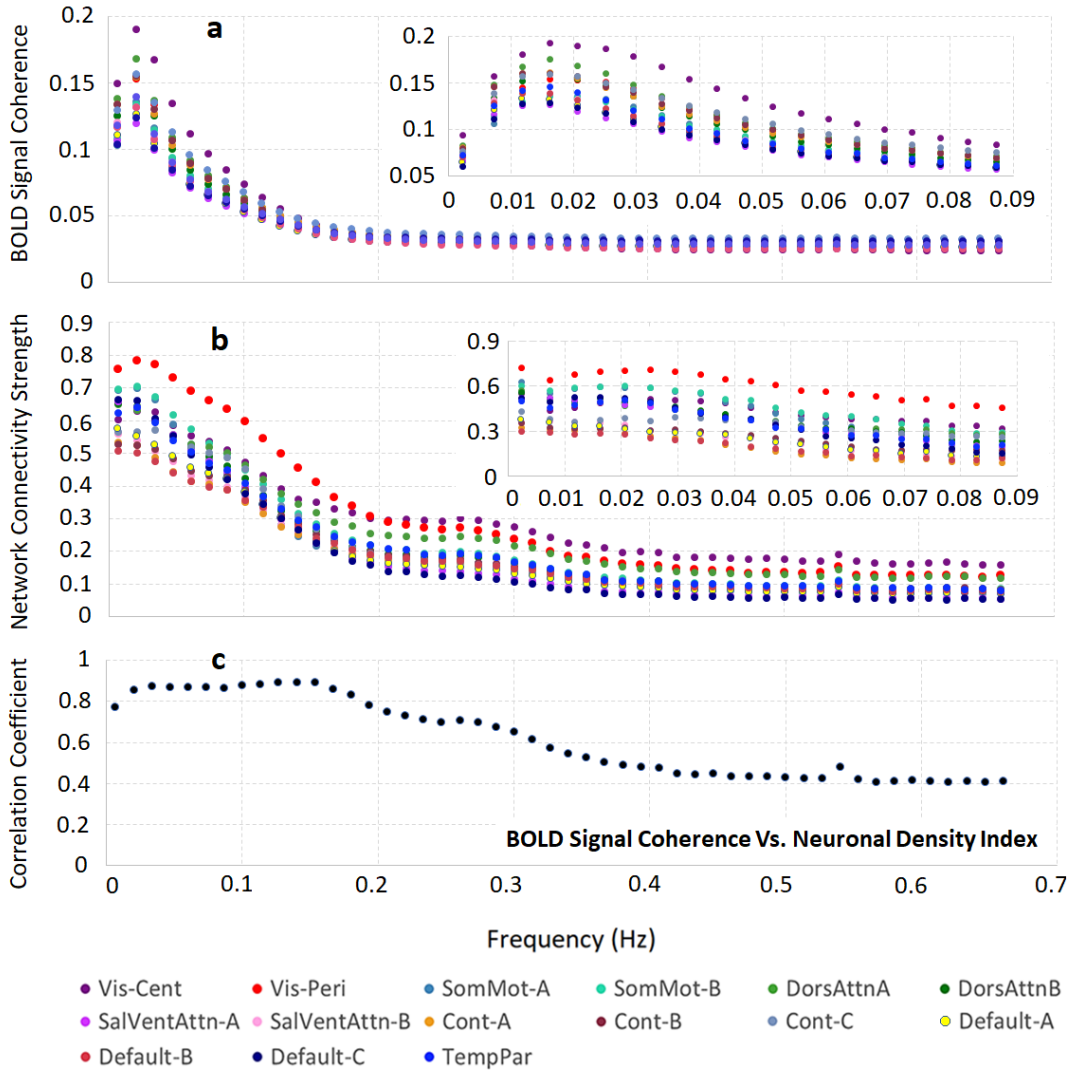

Figure 6. Relationship between frequency content of the resting state BOLD signal and the brain cellular structure. **(a)** BOLD signal coherence (mean standard deviations of the rs-fMRI signal) in 15 networks as a function of rs-fMRI signal frequency content. **(b)** The intra-network connectivity strength (NCS) of 15 networks as a function of rs-fMRI signal frequency content. Both panels **(a)** and **(b)** show relatively sharp peaks for all networks between 0.01 Hz and 0.03 Hz that are further illustrated in the insets. **(c)** Correlation coefficient between BOLD signal coherence in 15 networks and tissue neuronal content of these networks (as in **Figure 3**) as a function of rs-fMRI signal frequency content. The frequency resolution in main graphs is 0.014 Hz and in the inset it is 0.0047 Hz. Data show the strongest correlation in a rather broad infra-slow frequency range between 0.01 – 0.16 Hz.

DISCUSSION

While numerous specific mechanisms involved in neuronal signal transmission between different parts of the CNS are well understood, understanding the interrelationships between these mechanisms, and how they contribute to brain function, is still an elusive goal of neuroscience. A great number of papers are now devoted to one branch of this goal - studying brain functional networks reflecting intrinsic brain activity in the resting state (e.g. see (50) and references therein). While significant progress has been achieved in studying resting state functional networks in health and disease, many questions related to the relationship between resting state functional organization and underlying brain cellular organization are still not well understood.

Substantial advances in this direction have been achieved by utilizing information on brain genetic organization available from the Allen Human Brain Atlas (https://portal.brain-map.org/). Richiardi et al. (51) found that functional networks are underpinned by the networks of genes coding for ion channels and synaptic functions. Hawrylycz et al. (52) demonstrated that genes in the neuron-associated networks showed higher preservation between human brains and were related to functionally relevant circuitry. Furthermore, Goyal et al. (53) were able to differentiate between the use of aerobic glycolysis in networks, which was associated with the presence of genes related to synapse formation and growth (i.e., transcriptional neotony).

By using information on spatial distribution of gene expression profiles in human brain provided by the Allen Human Brain Atlas, Wen et al. (26) identified three *gene structural networks* related to brain neuronal, glia, and synaptic structures. Importantly, a strong association between these networks and the R2t* metric of the qGRE MRI signal (22) was established in (26). This showed that *in vivo* measurement of the major baseline tissue-cellular-specific component of qGRE signal decay rate parameter R2t* (t stands for tissue) provides a unique genetic perspective into the cellular constituents of the human cortex and can serve as a previously unidentified link between cortical tissue cellular composition and MRI signal. Analysis of the genetically-derived brain cellular composition (26) was in good agreement with direct histological measurements by Herculano-Houzel (54) and other previous findings (38,55,56).

It is worth noting that the method used in (26) to establish a relationship between R2t* metric and brain tissue neuronal density is not as different from traditional histology as one might think. Indeed, in traditional histology, an MRI metric (R2t* in our case) would be correlated with the count of a histological markers specific to mature neurons and other markers specific to other cells such as astrocytes, and to structural components such as myelin. In (26), instead of using histological markers, published gene expression profiles (Microarray Data :: Allen Brain Atlas: Human Brain (brain-map.org)) were used with their relationship to neurons established using available tools such as ToppGene portal (https:/toppgene.cchmc.org) which includes 19061 genes in the "Cellular Component" category and 23956 genes in the "Coexpression Atlas" category. The sensitivity of the gene enrichment analysis was demonstrated using DAVID Bioinformatics Resources (https://david.ncifcrf.gov/). Results showed that gene expression profiles affiliated with neuronal cellular and subcellular compartments correlated strongly with R2t*.

In this paper we use quantitative relationships established in (26) between the R2t* metric of the quantitative Gradient Recalled Echo (qGRE) MRI signal and the human brain cellular composition to study *in vivo* interrelationships between human brain resting state functional connectivity which is known

to provide insights into large-scale brain circuit organization (2,3) and underlying brain cellular organization.

Our functional connectivity analysis is based on the resting state data obtained from the HCP1200 dataset (February, 2017 release) of young adults aged between 22 and 35 (5). To analyze resting state functional connectivity data we use brain parcellation into individual functional units and brain resting state networks proposed in (7,30) that allow significant reduction of large volume of resting state functional connectivity data but also providing a sufficient number of parcels to delineate the importance of brain cortical anatomical structures as emphasized by Van Essen et al. (44).

Our results elucidate the relationship between the components of human brain cellular composition (neurons, glia cells and synapses) and the BOLD signal characteristics of the resting state functional networks. In our approach, the functional connectivity inside the individual functional units (ROIs) is characterized by the coherence of the BOLD signals from the voxels/vertices comprising functional units (Eq. [3]), while the intra-network functional connections are characterized by the coherence of the global BOLD signals generated by functional units comprising these networks (Eqs. [8], [9]). Our analysis reveals the relationships between brain functional properties and cellular content. The general trend indicates that the functional units with higher concentration of neurons and correspondingly lower concentration of glial cells and synapses display stronger coherence of the rs-fMRI BOLD signals in the individual functional units (**Figure 3** and **Figure A3 in the Appendix**). This result reveals that the synchrony of the connections between brain cellular circuits in individual functional units is mostly governed by the neurons – a higher concentration of neurons leads to stronger functional connections. At the same time, the synchrony of connections between cellular circuits belonging to different functional units in the network is largely governed, not only by the strength of the neuron-neuron associations between functional units, but also neuron-synapse, and neuron-glia associations (**Figure 4**).

The strong role of the neuronal-glia connection in forming strong network connections is also in agreement with the role that glial cells play by providing metabolic (57,58) and regulatory (59) support for neurons as well as support for neurite outgrowth and neuronal guidance (17,18). Moreover, neuron-glia cross-talk leads to synaptic formation and remodeling. In absence of glia, neurons generate weak synapses (17,21). The dependence of intra-network connectivity strength on the neuron-synapse relationship could also have been expected because they operate as a unit in conducting brain electric currents.

To further clarify the role that different parts of the neuron play in formation of brain functional connectivity, we can compare our R2t*-based results with a T1w/T2w-derived proxy related to the cortical tissue myelin content proposed (38) and successfully used (40) for mapping human cortical areas by Glasser and Van Essen. An association between T1w/T2w myelin proxy and gene profiles from an Allen Human Brain Atlas was also established in (60). Data in **Figure 5a** shows a very strong ($R^2 = 0.61$) correlation between measurements of the Neuronal Density Index (NDI) and T1w/T2w-derived Myelin Index (MI) across the 15 networks (Limbic networks were omitted from this consideration for the same reasons that R2t* and functional connectivity data were omitted). This result is consistent with previous findings that the neuronal densities tend to be higher in areas of high myelin content and low in areas of low myelin content (38,55) that have more complex intracortical circuitry (i.e. larger dendritic field sizes and larger dendritic arbors) (56). At the same time, data suggest that not all parts of the R2t*-based calculated NDI are associated with the presence of myelinated neuronal processes. These results are expected because *myelin covers only part of the neuron*, i.e. myelinated axons, while R2t*-based *NDI*

comprises all parts of neuronal structure, i.e., cell body, myelinated and not-myelinated axons, and dendrites.

The conclusion that the qGRE-derived NDI also has additional contributions of myelinated axons from remaining neuronal components – dendrites and soma – is further supported by data in **Figure 5b** and **Figure 5c**. Indeed, data in **Figure 5b** show that the correlation between BOLD signal coherence and Myelin Index is much weaker ($R^2 = 0.23$) than the correlation between BOLD signal coherence and NDI ($R^2 = 0.51$, **Figure 3**). Subsequently, comparison of data in **Figure 4** and **Figure 5c** shows that the intra-network connectivity strength has stronger association with neuron-neuron connections ($R^2 = 0.53$) than with the connections due to the myelinated processes ($R^2 = 0.47$). This might suggest that the qGRE NDI metric has a stronger association with the brain cellular "functionality" than the T1w/T2w-derived myelin index. These results are quite instructive. They suggest that the BOLD signal coherence in the individual brain ROIs comprising functional connectivity networks might be mostly associated with the non-myelinated parts of the neurons – dendrites and soma. At the same time, the inter-ROIs connectivity has significantly stronger contribution from myelinated axons needed to secure inter-unit, within-network functional connectivity.

In this paper we have also provided a detailed analysis of the "frequency content" of the resting state BOLD signal and a corresponding strength of the resting state functional connectivity in relation to the underlying cellular composition. It is well appreciated that the resting state BOLD signal originates from a specific element of brain activity, i.e., *infra-slow* activity with frequencies approximately below 0.1 Hz which is thought to be linked in this interval to the neuronal activities (3,45-49). Our data are in agreement with this notion – for all networks, the resting state BOLD signal coherence and the intra-network connectivity strength are not monotonic functions of the frequency with a rather sharp peaks in the *infra-slow frequency* range between 0.01 and 0.16 Hz (**Figure 6a** and **Figure 6b**). A relationship of these infra-slow BOLD signal fluctuations to neuronal activity is clearly supported by a plot in **Figure 6c** showing a high correlation plateau in the frequency range of 0.01 to 0.16 Hz on the curve displaying correlation between Neuronal Density Index and BOLD signal coherence.

All these mechanisms lead to a rather broad distribution of resting state functional networks' properties. We found that the visual networks express the highest neuronal density, yet lowest density of glial cells and synapses, and the strongest intra-functional-unit BOLD signal coherence and intra-network connectivity. The DMN shows relatively low intra-functional-unit BOLD signal coherence and intra-network connectivity strength, but significant diversity of cellular constituents. The DMN part B exhibits a remarkably balanced cellular content – Neuronal Density Index (0.51) was almost exactly equal to Glia Density (0.49) and Synaptic Density (0.48) indices. At the same time, the other parts of DMN (A and C) that include temporal and inferior parietal lobules, dorsal prefrontal, precuneus posterior cingulate, medial prefrontal, retrosplenial, and parahippocampal cortices have more condensed neuronal content with relatively lower concentration of synapses and glia cells. This network is affiliated with temporal, inferior parietal, dorsal prefrontal, lateral prefrontal, and ventral prefrontal brain regions. These results can potentially be helpful in understanding the unique features of DMN and its very prominent role in the overall organization of the brain (61) plus it's the target of Alzheimer disease (62).

As the study of resting state functional connectivity within and among the large networks of the human brain has moved forward, the concept of hierarchies among these networks has emerged as a major area of interest (for example see (48,63) and the references therein). Broadly speaking, networks are positioned according to a variety of features beginning with the sensorimotor cortices and ascending to association cortices with the brain's default mode network at the top of this hierarchy. Networks at the top of the hierarchy are less myelinated (64), exhibit higher levels of aerobic glycolysis (65,66) and harbor neotenous genes (67). Together these features relate to the presence of synapses and their role in growth and plasticity. Our data would add that networks at the top of the hierarchy have more dense synaptic relative to neuronal structure (see **Figure 2**). This may be relevant to our understanding of a functional feature of networks at the top of the hierarchy as they integrate incoming information more slowly than, for example, primary sensory areas (48,68).

CONCLUSION

In this paper we have provided a detailed analysis of the associations between human brain cellular composition and functional networks identified by the resting state BOLD signal. Our results show that the brain regions with higher concentration of neurons, but relatively lower concentration of glial cells and synapses support strong connections between cellular circuits in the network-defined functional units, leading to the strong BOLD signal coherence in individual functional units. Furthermore, our results show that a significant contribution to a between-unit connectivity is provided by the neuron-neuron, neuron-synaptic, and neuron-glia connections between cellular circuits.

These relationships lead to a rather broad distribution of the resting state functional networks' properties. We found that the visual networks have the strongest BOLD signal coherence with the highest neuronal density (but lowest density of glial cells and synapses), and the strongest intra-network connectivity. The Default Mode Network (DMN) shows relatively low BOLD signal coherence and Network Connectivity Strength but significant diversity of cellular circuits reflecting the DMN's prominent role in the overall organization of the brain and the hierarchy of functional networks.

ACKNOWLEDGEMENT This study was supported by the NIH grant R01 AG054513. The resting state data of this study were provided by the Human Connectome Project, WU-Minn Consortium (Principal Investigators: David Van Essen and Kamil Ugurbil; 1U54MH091657) funded by the 16 NIH Institutes and Centers that support the NIH Blueprint for Neuroscience Research; and by the McDonnell Center for Systems Neuroscience at Washington University. The genetic information was obtained from Allen Institute for Brain Science, Allen Human Brain Atlas, Available from: human.brain-map.org. The authors would also like to acknowledge helpful discussions at different stages of this project with Charles Hildebolt, Dillan Newbold, Reza Hamidian, Janine Bijsterbosch, BT Thomas Yeo and Ryan Raut. Editing assistance was provided by InPrint: A Scientific Editing Network at Washington University in St. Louis.

APPENDIX

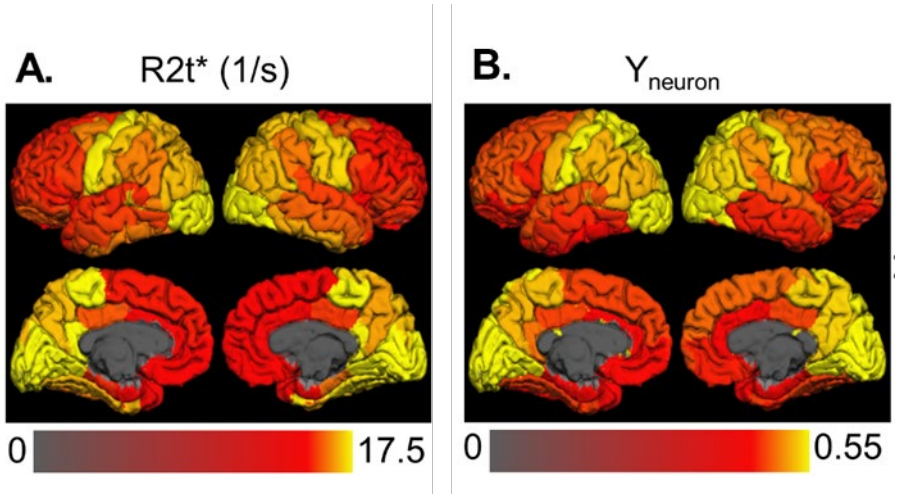

Figure A1. The association between the expression of neuron-related genetic network across different regions of the human brain and R2t* measurements in the same regions (adapted from (26)). R2t* map (**A**) in this figure is obtained from qGRE MRI; Yneuron (**B**) (designated as Neuronal Density Index) is obtained from the analysis of the gene expression profiles in the Allen Human Brain Atlas – two totally independent measurements. The figure and analysis in (26) provided convincing and consistent with literature arguments that the R2t* metric of qGRE signal is strongly associated with the neuronal density.

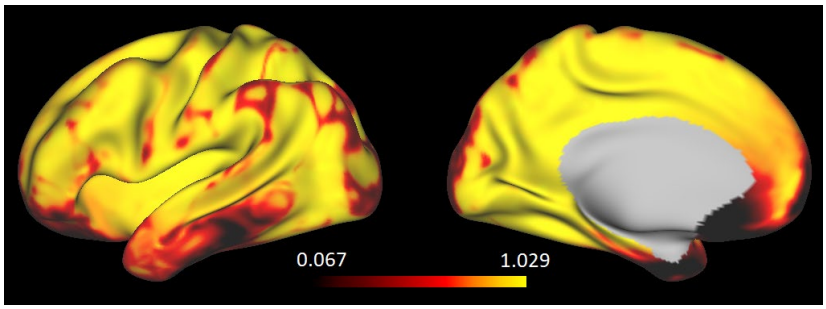

Figure A2. Map characterizing magnetic field inhomogeneities in the human brain obtained from the phase information of qGRE signal by means of the Voxel Spread Function approach (33). Yellow color designates areas lightly affected by magnetic field inhomogeneities. Black color designates severely affected areas. The scale bar shows values of the so-called F-function (33) at the gradient echo time TE =40 ms. F-function shows fraction of signal not affected by the loss due to the field inhomogeneities, ranging from 1 (no signal loss) to 0 (full loss of signal). Images show significant loss of signal in both Limbic networks, thus adversely affecting quantitative analysis of both, rs-fMRI and qGRE data.

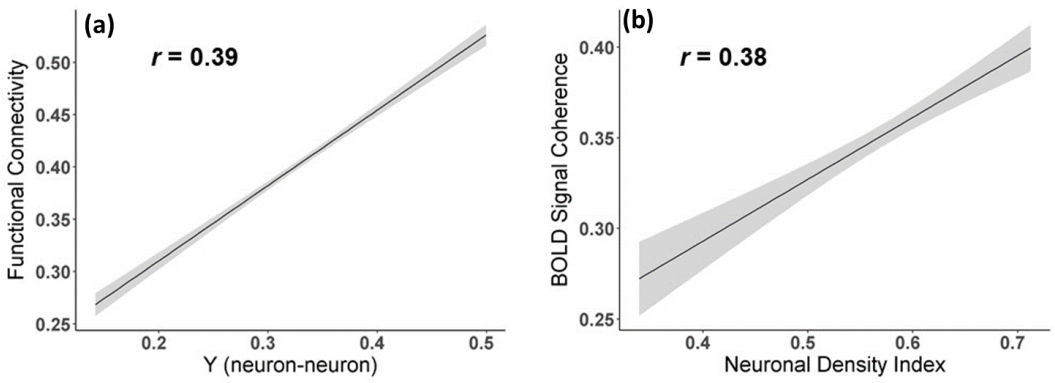

Figure A3. (a): Association between Functional Connectivity Strength defined based on 280 ROIs and structural connectivity between neurons in these ROIs. The correlation is highly significant with p= 9 E-98**; (b):** Association between BOLD signal coherence in 280 ROIs and neural density index in these ROIs. The correlation is highly significant with p= 5.3 E-11. In both curves ROIs in limbic networks are omitted. Shaded areas – 95% confidence intervals. Actual data are not shown due to their big number.

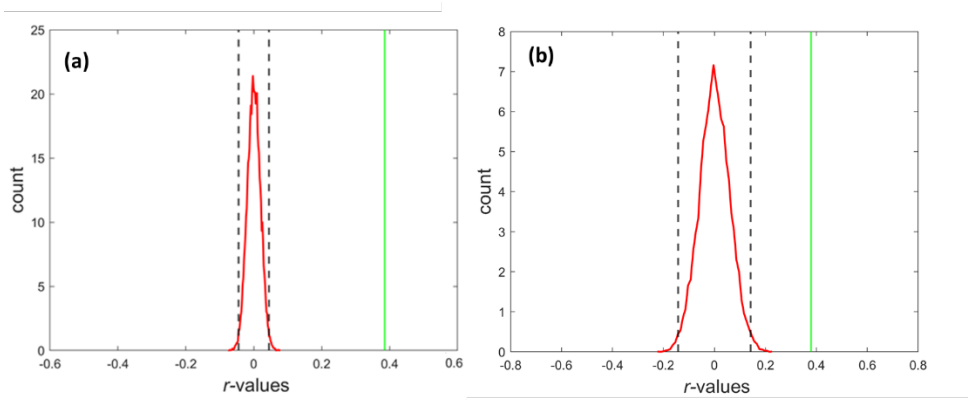

Figure A4. Permutation Test Analysis (randomization test). (a): Functional Connectivity vs. Structural Connectivity between neurons, Y (neuron-neuron). The curve shows the distribution of *r*-values calculated between Y (neuron-neuron) and randomly permuting FC 20000 times. **(b)**: BOLD Signal Coherence vs. Neuronal Density Index (NDI). The curve shows the distribution of *r*-values calculated between NDI and randomly permuting 10000 times BOLD Signal Coherence.
In both plots, the 99% percentiles of the distribution lines are marked by black dashed lines, the r-values without permutation are marked as green lines and are well outside black lines. The result shown in the figures validates a significant difference in both cases with p-values <0.000001).

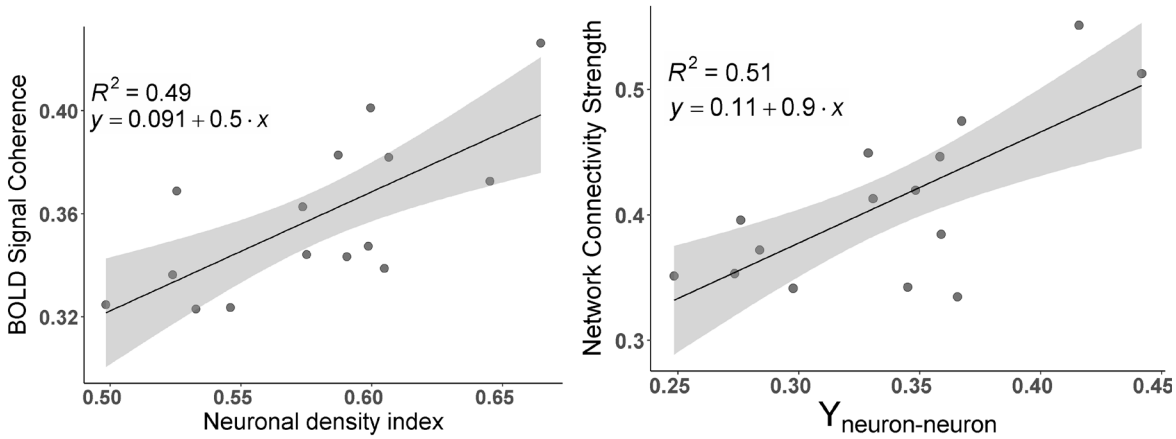

Figure A5. Statistical sufficiency of sample size. To demonstrate statistical sufficiency of our sample size (N=183) we have run analysis similar to presented in **Figure 3** and **Figure 4** using a smaller sample size (N = 100). Results presented herein in **Figure A5** show practically the same correlations with only slightly smaller R^2 values.

NETWORKS	R2t* Mean	R2t* STD	NDI	GDI	SDI
Vis-Cent	19.67	0.8	0.66	0.44	0.42
Vis-Peri	18.86	0.48	0.65	0.45	0.43
SomMot-A	16.95	0.82	0.58	0.47	0.45
SomMot-B	18.02	0.78	0.6	0.46	0.44
DorsAttnA	17.88	0.67	0.61	0.46	0.44
DorsAttnB	17.13	0.79	0.57	0.47	0.45
SalVentAttn-A	16.61	0.68	0.53	0.49	0.47
SalVentAttn-B	16.34	0.71	0.52	0.49	0.47
Cont-A	17.69	0.73	0.59	0.47	0.45
Cont-B	16.55	0.74	0.53	0.49	0.47
Cont-C	17.87	0.96	0.6	0.46	0.44
Default-A	16.6	0.71	0.55	0.48	0.47
Default-B	16.29	0.83	0.5	0.5	0.49
Default-C	18.06	0.71	0.6	0.49	0.44
TempPar	17.81	0.68	0.59	0.47	0.45

Table A. Summary of R2t* and cellular densities in 15 networks.
Columns 2 and 3 represent Mean and Standard deviation of R2t* distribution across 16 subjects (values are in 1/sec). Columns 4-6 represent mean values of neuronal, glia and synaptic density indices (qGRE proxy for the neuronal (NDI), synaptic (SDI) and glia (GDI) cells densities). Data in columns 4-6 correspond to the maps in **Figure 2**.

REFERENCES

1. Biswal B, Yetkin FZ, Haughton VM, Hyde JS. Functional connectivity in the motor cortex of resting human brain using echo-planar MRI. Magn Reson Med 1995;34(4):537-541.
2. Buckner RL, Krienen FM, Yeo BTT. Opportunities and limitations of intrinsic functional connectivity MRI. Nat Neurosci 2013;16(7):832-837.
3. Fox MD, Raichle ME. Spontaneous fluctuations in brain activity observed with functional magnetic resonance imaging. Nat Rev Neurosci 2007;8(9):700-711.
4. Ogawa S, Lee TM, Kay AR, Tank DW. Brain magnetic resonance imaging with contrast dependent on blood oxygenation. Proc Natl Acad Sci U S A 1990;87(24):9868-9872.
5. Van Essen DC, Smith SM, Barch DM, Behrens TEJ, Yacoub E, Ugurbil K, Consortium W-MH. The WU-Minn Human Connectome Project: An overview. Neuroimage 2013;80:62-79.
6. Damoiseaux JS, Rombouts SA, Barkhof F, Scheltens P, Stam CJ, Smith SM, Beckmann CF. Consistent resting-state networks across healthy subjects. Proc Natl Acad Sci U S A 2006;103(37):13848-13853.
7. Yeo BT, Krienen FM, Sepulcre J, Sabuncu MR, Lashkari D, Hollinshead M, Roffman JL, Smoller JW, Zollei L, Polimeni JR, Fischl B, Liu H, Buckner RL. The organization of the human cerebral cortex estimated by intrinsic functional connectivity. J Neurophysiol 2011;106(3):1125-1165.
8. Andrews-Hanna JR, Snyder AZ, Vincent JL, Lustig C, Head D, Raichle ME, Buckner RL. Disruption of large-scale brain systems in advanced aging. Neuron 2007;56(5):924-935.
9. Buckner RL, Snyder AZ, Shannon BJ, LaRossa G, Sachs R, Fotenos AF, Sheline YI, Klunk WE, Mathis CA, Morris JC, Mintun MA. Molecular, structural, and functional characterization of Alzheimer's disease: evidence for a relationship between default activity, amyloid, and memory. J Neurosci 2005;25(34):7709-7717.
10. De Luca M, Beckmann CF, De Stefano N, Matthews PM, Smith SM. fMRI resting state networks define distinct modes of long-distance interactions in the human brain. Neuroimage 2006;29(4):1359-1367.
11. Greicius MD, Supekar K, Menon V, Dougherty RF. Resting-state functional connectivity reflects structural connectivity in the default mode network. Cereb Cortex 2009;19(1):72-78.
12. Toosy AT, Ciccarelli O, Parker GJM, Wheeler-Kingshott CAM, Miller DH, Thompson AJ. Characterizing function-structure relationships in the human visual system with functional MRI and diffusion tensor imaging. Neuroimage 2004;21(4):1452-1463.
13. Uddin LQ. Complex relationships between structural and functional brain connectivity. Trends Cogn Sci 2013;17(12):600-602.
14. Honey CJ, Sporns O, Cammoun L, Gigandet X, Thiran JP, Meuli R, Hagmann P. Predicting human resting-state functional connectivity from structural connectivity. P Natl Acad Sci USA 2009;106(6):2035-2040.
15. Ding Z, Huang Y, Bailey SK, Gao Y, Cutting LE, Rogers BP, Newton AT, Gore JC. Detection of synchronous brain activity in white matter tracts at rest and under functional loading. Proc Natl Acad Sci U S A 2018;115(3):595-600.
16. Fields RD, Woo DH, Basser PJ. Glial Regulation of the Neuronal Connectome through Local and Long-Distant Communication. Neuron 2015;86(2):374-386.
17. Pannasch U, Vargova L, Reingruber J, Ezan P, Holcman D, Giaume C, Sykova E, Rouach N. Astroglial networks scale synaptic activity and plasticity. Proc Natl Acad Sci U S A 2011;108(20):8467-8472.
18. Ullian EM, Sapperstein SK, Christopherson KS, Barres BA. Control of synapse number by glia. Science 2001;291(5504):657-661.
19. Pellerin L, Magistretti PJ. Sweet sixteen for ANLS. J Cereb Blood Flow Metab 2012;32(7):1152-1166.
20. Stogsdill JA, Eroglu C. The interplay between neurons and glia in synapse development and plasticity. Curr Opin Neurobiol 2017;42:1-8.

21. Araque A, Navarrete M. Glial cells in neuronal network function. Philos Trans R Soc Lond B Biol Sci 2010;365(1551):2375-2381.
22. Ulrich X, Yablonskiy DA. Separation of cellular and BOLD contributions to T2* signal relaxation. Magn Reson Med 2016;75(2):606-615.
23. Yablonskiy DA, Haacke EM. Theory of NMR signal behavior in magnetically inhomogeneous tissues: the static dephasing regime. Magn Reson Med 1994;32(6):749-763.
24. Yablonskiy DA. Quantitation of intrinsic magnetic susceptibility-related effects in a tissue matrix. Phantom study. Magn Reson Med 1998;39(3):417-428.
25. Yablonskiy DA, Sukstanskii AL, Luo J, Wang X. Voxel spread function method for correction of magnetic field inhomogeneity effects in quantitative gradient-echo-based MRI. Magn Reson Med 2013;70(5):1283-1292.
26. Wen J, Goyal MS, Astafiev SV, Raichle ME, Yablonskiy DA. Genetically defined cellular correlates of the baseline brain MRI signal. Proc Natl Acad Sci U S A 2018;115(41):E9727-E9736.
27. Herculano-Houzel S. The glia/neuron ratio: How it varies uniformly across brain structures and species and what that means for brain physiology and evolution. 2014;62(9):1377-1391.
28. Cullen DK, Gilroy ME, Irons HR, Laplaca MC. Synapse-to-neuron ratio is inversely related to neuronal density in mature neuronal cultures. Brain Res 2010;1359:44-55.
29. Glasser MF, Sotiropoulos SN, Wilson JA, Coalson TS, Fischl B, Andersson JL, Xu J, Jbabdi S, Webster M, Polimeni JR, Van Essen DC, Jenkinson M, Consortium WU-MH. The minimal preprocessing pipelines for the Human Connectome Project. Neuroimage 2013;80:105-124.
30. Schaefer A, Kong R, Gordon EM, Laumann TO, Zuo XN, Holmes AJ, Eickhoff SB, Yeo BTT. Local-Global Parcellation of the Human Cerebral Cortex from Intrinsic Functional Connectivity MRI. Cereb Cortex 2018;28(9):3095-3114.
31. Zhao Y, Wen J, Cross AH, Yablonskiy DA. On the relationship between cellular and hemodynamic properties of the human brain cortex throughout adult lifespan. Neuroimage 2016;133:417-429.
32. Wen J, Cross AH, Yablonskiy DA. On the Role of Physiological Fluctuations in Quantitative Gradient Echo MRI: Implications for GEPCI, QSM, and SWI. Magnetic Resonance in Medicine 2015;73(1):195-203.
33. Yablonskiy DA, Sukstanskii AL, Luo J, Wang XQ. Voxel Spread Function Method for Correction of Magnetic Field Inhomogeneity Effects in Quantitative Gradient-Echo-Based MRI. Magnetic Resonance in Medicine 2013;70(5):1283-1292.
34. Quirk JD, Sukstanskii AL, Bretthorst GL, Yablonskiy DA. Optimal decay rate constant estimates from phased array data utilizing joint Bayesian analysis. Journal of Magnetic Resonance 2009;198(1):49-56.
35. Luo J, Jagadeesan BD, Cross AH, Yablonskiy DA. Gradient echo plural contrast imaging—signal model and derived contrasts: T2*, T1, phase, SWI, T1f, FST2* and T2*-SWI. Neuroimage 2012;60(2):1073-1082.
36. Yablonskiy DA. Quantitation of intrinsic magnetic susceptibility-related effects in a tissue matrix. Phantom study. Magnetic resonance in medicine 1998;39(3):417-428.
37. Yablonskiy DA, Sukstanskii AL, He X. Blood oxygenation level-dependent (BOLD)-based techniques for the quantification of brain hemodynamic and metabolic properties - theoretical models and experimental approaches. NMR Biomed 2013;26(8):963-986.
38. Glasser MF, Van Essen DC. Mapping Human Cortical Areas In Vivo Based on Myelin Content as Revealed by T1- and T2-Weighted MRI. Journal of Neuroscience 2011;31(32):11597-11616.
39. Lazari A, Lipp I. Can MRI measure myelin? Systematic review, qualitative assessment, and meta-analysis of studies validating microstructural imaging with myelin histology. NeuroImage 2021;230:117744.
40. Glasser MF, Coalson TS, Robinson EC, Hacker CD, Harwell J, Yacoub E, Ugurbil K, Andersson J, Beckmann CF, Jenkinson M, Smith SM, Van Essen DC. A multi-modal parcellation of human cerebral cortex. Nature 2016;536(7615):171-+.
41. Craddock RC, James GA, Holtzheimer PE, Hu XPP, Mayberg HS. A whole brain fMRI atlas generated via spatially constrained spectral clustering. Hum Brain Mapp 2012;33(8):1914-1928.

42. Gordon EM, Laumann TO, Adeyemo B, Huckins JF, Kelley WM, Petersen SE. Generation and Evaluation of a Cortical Area Parcellation from Resting-State Correlations. Cerebral Cortex 2016;26(1):288-303.
43. Shen X, Tokoglu F, Papademetris X, Constable RT. Groupwise whole-brain parcellation from resting-state fMRI data for network node identification. Neuroimage 2013;82:403-415.
44. Van Essen DC, Glasser MF, Dierker DL, Harwell J, Coalson T. Parcellations and hemispheric asymmetries of human cerebral cortex analyzed on surface-based atlases. Cereb Cortex 2012;22(10):2241-2262.
45. Han Y, Wang JH, Zhao ZL, Min BQ, Lu J, Li KC, He Y, Jia JP. Frequency-dependent changes in the amplitude of low-frequency fluctuations in amnestic mild cognitive impairment: A resting-state fMRI study. Neuroimage 2011;55(1):287-295.
46. Mitra A, Kraft A, Wright P, Acland B, Snyder AZ, Rosenthal Z, Czerniewski L, Bauer A, Snyder L, Culver J, Lee JM, Raichle ME. Spontaneous Infra-slow Brain Activity Has Unique Spatiotemporal Dynamics and Laminar Structure. Neuron 2018;98(2):297-+.
47. Palva JM, Palva S. Infra-slow fluctuations in electrophysiological recordings, blood-oxygenation-level-dependent signals, and psychophysical time series. Neuroimage 2012;62(4):2201-2211.
48. Raut RV, Snyder AZ, Raichle ME. Hierarchical dynamics as a macroscopic organizing principle of the human brain. Proc Natl Acad Sci U S A 2020;117(34):20890-20897.
49. Zhang DY, Raichle ME. Disease and the brain's dark energy. Nat Rev Neurol 2010;6(1):15-28.
50. Raichle ME. The restless brain: how intrinsic activity organizes brain function. Philos T R Soc B 2015;370(1668):82-92.
51. Richiardi J, Altmann A, Milazzo AC, Chang C, Chakravarty MM, Banaschewski T, Barker GJ, Bokde ALW, Bromberg U, Buchel C, Conrod P, Fauth-Buhler M, Flor H, Frouin V, Gallinat J, Garavan H, Gowland P, Heinz A, Lemaitre H, Mann KF, Martinot JL, Nees F, Paus T, Pausova Z, Rietschel M, Robbins TW, Smolka MN, Spanagel R, Strohle A, Schumann G, Hawrylycz M, Poline JB, Greicius MD, Consortium I. Correlated gene expression supports synchronous activity in brain networks. Science 2015;348(6240):1241-1244.
52. Hawrylycz M, Miller JA, Menon V, Feng D, Dolbeare T, Guillozet-Bongaarts AL, Jegga AG, Aronow BJ, Lee CK, Bernard A, Glasser MF, Dierker DL, Menche J, Szafer A, Collman F, Grange P, Berman KA, Mihalas S, Yao ZZ, Stewart L, Barabasi AL, Schulkin J, Phillips J, Ng L, Dang C, Haynor DR, Jones A, Van Essen DC, Koch C, Lein E. Canonical genetic signatures of the adult human brain. Nat Neurosci 2015;18(12):1832-1844.
53. Goyal MS, Hawrylycz M, Miller JA, Snyder AZ, Raichle ME. Aerobic Glycolysis in the Human Brain Is Associated with Development and Neotenous Gene Expression. Cell Metab 2014;19(1):49-57.
54. Herculano-Houzel S. The Glia/Neuron Ratio: How it Varies Uniformly Across Brain Structures and Species and What that Means for Brain Physiology and Evolution. Glia 2014;62(9):1377-1391.
55. Collins CE, Airey DC, Young NA, Leitch DB, Kaas JH. Neuron densities vary across and within cortical areas in primates. P Natl Acad Sci USA 2010;107(36):15927-15932.
56. Elston GN, Benavides-Piccione R, DeFelipe J. The pyramidal cell in cognition: A comparative study in human and monkey. Journal of Neuroscience 2001;21(17).
57. Magistretti PJ, Allaman I. A Cellular Perspective on Brain Energy Metabolism and Functional Imaging. Neuron 2015;86(4):883-901.
58. Suzuki A, Stern SA, Bozdagi O, Huntley GW, Walker RH, Magistretti PJ, Alberini CM. Astrocyte-Neuron Lactate Transport Is Required for Long-Term Memory Formation. Cell 2011;144(5):810-823.
59. Poskanzer KE, Yuste R. Astrocytic regulation of cortical UP states. P Natl Acad Sci USA 2011;108(45):18453-18458.
60. Burt JB, Demirtas M, Eckner WJ, Navejar NM, Ji JL, Martin WJ, Bernacchia A, Anticevic A, Murray JD. Hierarchy of transcriptomic specialization across human cortex captured by structural neuroimaging topography. Nat Neurosci 2018;21(9):1251-+.
61. Margulies DS, Ghosh SS, Goulas A, Falkiewicz M, Huntenburg JM, Langs G, Bezgin G, Eickhoff SB, Castellanos FX, Petrides M, Jefferies E, Smallwood J. Situating the default-mode network along a principal gradient of macroscale cortical organization. 2016;113(44):12574-12579.

62. Palmqvist S, Schöll M, Strandberg O, Mattsson N, Stomrud E, Zetterberg H, Blennow K, Landau S, Jagust W, Hansson O. Earliest accumulation of β-amyloid occurs within the default-mode network and concurrently affects brain connectivity. Nature Communications 2017;8(1):1214.
63. Huntenburg JM, Bazin PL, Margulies DS. Large-Scale Gradients in Human Cortical Organization. Trends Cogn Sci 2018;22(1):21-31.
64. Glasser MF, Goyal MS, Preuss TM, Raichle ME, Van Essen DC. Trends and properties of human cerebral cortex: Correlations with cortical myelin content. NeuroImage 2014;93:165-175.
65. Vaishnavi SN, Vlassenko AG, Rundle MM, Snyder AZ, Mintun MA, Raichle ME. Regional aerobic glycolysis in the human brain. 2010;107(41):17757-17762.
66. Glasser MF, Goyal MS, Preuss TM, Raichle ME, Van Essen DC. Trends and properties of human cerebral cortex: Correlations with cortical myelin content. Neuroimage 2013.
67. Goyal MS, Hawrylycz M, Miller JA, Snyder AZ, Raichle ME. Aerobic glycolysis in the human brain is associated with development and neotenous gene expression. Cell Metab 2014;19(1):49-57.
68. Chaudhuri R, Knoblauch K, Gariel MA, Kennedy H, Wang XJ. A Large-Scale Circuit Mechanism for Hierarchical Dynamical Processing in the Primate Cortex. Neuron 2015;88(2):419-431.